Journal of Alloys and Metallurgical Systems 5 (2024) 100063

Contents lists available at ScienceDirect

Journal of Alloys and Metallurgical Systems

journal homepage: www.journals.elsevier.com/journal-of-alloys-and-metallurgical-systems

Direct artificial aging of the PBF-LB AlSi10Mg alloy designed to enhance the trade-off between strength and residual stress relief

Gianluca Di Egidio *, Lavinia Tonelli *, Mattia Zanni, Daniele Carosi, Alessandro Morri, Lorella Ceschini

Department of Industrial Engineering (DIN), Alma Mater Studiorum, University of Bologna, Viale del Risorgimento 4, Bologna 40136, Italy

ARTICLE INFO

Keywords:
Additive manufacturing
Aluminum alloys
Microstructure
Residual stress
Mechanical properties
Heat treatment

ABSTRACT

The AlSi10Mg alloy is one of the most studied alloys processed by the Powder Bed Fusion-Laser Beam (PBF-LB). Many already published works focus on post-process heat treatments to reduce residual stress or improve mechanical strength. Instead, the present study aims to identify direct artificial aging (AA) heat treatment able to optimize both aspects, thus enhancing the trade-off between strengthening and residual stress relief for the PBF-LB AlSi10Mg alloy produced using a no-heated platform. Higher temperatures (190–240 °C) than those typically used in AA heat treatment were selected based on thermal analysis to benefit both residual stress relief and precipitation of reinforcing phases from the supersaturated solid solution of the metastable as-built alloy. The effects of AA heat treatment on mechanical properties (i.e. hardness) and residual stress were evaluated by plotting aging curves and by XRD and Raman analyses and demonstrated that different trade-offs between strengthening and stress relief can be achieved by tuning heat treatment parameters (temperature and time). In particular, the exposure at the lowest temperature (190 °C) induced a partial decrease in residual stress and a slight increase in hardness. By increasing heat treatment temperature and soaking time, the relief was more significant, whilst the decrease in hardness was rather limited. The results are supported by the microstructural changes observed on the samples due to the different heat treatment conditions applied and show the feasibility of designing an AA heat treatment for the PBF-LB AlSi10Mg alloy capable of satisfying the mechanical response required by the final application.

1. Introduction

In recent years, several Additive Manufacturing (AM) processes based on a layer-by-layer strategy have been developed as an alternative to traditional subtractive or joining manufacturing methodologies. In this context, Powder Bed Fusion-Laser Beam (PBF-LB) represents one of the most interesting technologies currently available [1,2]. Following a pre-defined scan strategy, PBF-LB uses a high-energy-density laser beam to selectively melt a metallic powder bed deposited on the building platform. This printing system creates customizable geometries, reduces manufacturing time and raw material consumption, and improves the specific mechanical performance of the parts by significant weight reduction [3]. The features of the PBF-LB make the process highly suitable to meet the increasing demand from high-tech industries (aerospace, automotive, energy, and biomedical) for its flexibility in producing high-performance and custom-made components [4].

The AlSi10Mg alloy, a heat-treatable Al alloy, has recently been the subject of in-depth academic research to evaluate its large-scale application in the PBF-LB process [5]. The almost eutectic composition of the AlSi10Mg alloy ensures good processability thanks to a low hot-cracking tendency and a narrowed solidification range. At the same time, the relatively high Mg content promotes the precipitation of Mg_2Si reinforcing precipitates during manufacturing and heat treatment processes [6].

The specific process conditions of the PBF-LB technology and the physicochemical properties of the AlSi10Mg alloy influence the solidification structures of the microstructure [7]. The interaction between the laser beam and the Al powder leads to the melting of a small volume of material in the melt pool that rapidly solidifies in conditions far from equilibrium. The high solidification rate (10^3 - 10^8 K/s) leads to an extended solid solubility of Si into the Al lattice, inducing the formation of a metastable ultrafine cellular structure consisting of submicrometric

* Corresponding authors.
E-mail addresses: gianluca.diegidio2@unibo.it (G. Di Egidio), lavinia.tonelli2@unibo.it (L. Tonelli).

https://doi.org/10.1016/j.jalmes.2024.100063
Received 18 September 2023; Received in revised form 9 February 2024; Accepted 12 February 2024
Available online 17 February 2024

cells of supersaturated α-Al surrounded by a eutectic-Si network. This as-built microstructure (AB) is metastable and tends to evolve towards a more stable condition when subjected to high temperatures, thus modifying the mechanical response of the alloy [8,9]. Moreover, because the laser source melts only a localized volume of the powder bed, the surrounding area is subject to a step spatial thermal gradient and repeated heating and cooling cycles that determine a cyclic thermal expansion/contraction of the material and cause high residual stresses (RS) in the AB [10,11].

RS are classified according to magnitude and extension [12]: (i) Type I, macroscopic RS equal to the component size scale; (ii) Type II, intergranular RS due to the presence of different phases and local microstructural inhomogeneities; (iii) Type III, atomic scale RS resulting from the presence of lattice defects. In the worst cases, Type I RS directly lead to distortion or cracks in the parts. In contrast, Type II RS and Type III RS nearly always exist in polycrystalline materials due to differences in thermal and elastic properties among phases, differently oriented grains, and the presence of vacancies and interstitial or substitutional atoms inside the matrix crystal lattice [13].

In recent years, several authors have systematically studied the process conditions to control and reduce the RS during the PBF-LB process by focusing mainly on the process parameters, such as laser source, scanning strategy, powder bed characteristics, and component geometry [10,14]. Even though optimizing process parameters reduces part deformation and cracking, high levels of RS persist [15]. For these reasons, two new strategies have been developed to address this problem: (i) heating of the building platform and (ii) application of specific post-process heat treatments [16–18].

Heating the building platform between 80 and 200 °C [16,18–20] is a quite convenient strategy to reduce RS, distortions, and hot-tearing cracks by toning down the thermal gradient in the parts. Concurrently, the fluidity of the liquid metal increases, thus affecting microstructural features by reducing the formation of hot cracking and lack-of-fusion but raising the level of gas pore content due to the higher gas solubility in liquid metal [21,22]. However, as the alloy is exposed at a relatively high temperature for the whole process, a heated platform induces "in-situ" aging and microstructural coarsening of the AB [20], whilst the mechanical properties are closely related to the distance from the platform. As Amir et al. [23] and Cerri et al. [19] observed, the hardness and mechanical strength of the alloy increase proportionally with the distance from the building platform, introducing a source of anisotropy in the mechanical response of the component.

Stress relieving (SR), generally performed at 300 °C for a soaking time of up to 2 h [24–27], has been widely used to reduce the RS and improve the ductility of the alloy [11,28]. However, a significant loss in mechanical strength characterizes the stress-relieved alloy due to the complete modification of the microstructure induced by the thermal diffusion processes [29–31]. In particular, the thermal exposure during the SR breaks down the ultrafine eutectic-Si network of the AB alloy and leads to the formation of a composite-like microstructure consisting of globular Si-rich particles incorporated in the α-Al matrix.

Recently, attention has been paid to post-process heat treatments capable of inducing relief of RS by preserving good mechanical properties. One of the most interesting solutions is direct artificial aging (AA), performed at a temperature (T_{AA}) between 150 °C and 250 °C with a soaking time (t_{AA}) between 1 and 6 h [19,20,24–28,30,32]. However, AA is usually applied at 160 °C - 180 °C, known as T5 heat treatment, mainly to improve mechanical strength [20,26,32,33], whilst its potential in decreasing RS is not yet fully exploited. It promotes mechanical strengthening due to the precipitation of nano-sized Si particles and precursors of the Mg_2Si equilibrium phase by preserving the ultrafine microstructure of the AB alloy [19,30]. Still, it could also effectively reduce RS if the heat treatment parameters are appropriately chosen.

According to Fiocchi et al. [17,30], the effects of AA strictly depend on heat treatment conditions. By comparison to the AB alloy, they evidenced: (i) a decrease in RS of 80%, a negligible strength reduction, and an unaffected ductility after 3 h at 244 °C; (ii) a decrease in RS of 35% and an increase in hardness after 1.5 h at 170 °C, as also observed by the authors in previous work [24]. These preliminary results suggest temperatures higher than conventional AA heat treatments ($T_{AA} > 180$ °C) are needed to relieve stress significantly.

Despite the great potential of AA, supported by the literature mentioned above, data regarding the optimization of temperature and soaking time to reduce RS are currently quite limited. In this view, the present work aims to systematically analyze post-process AA and design it to enhance the trade-off between stress relief and mechanical strength (i.e., hardness). For this purpose, temperatures higher than 180 °C (T_{AA} = 190 °C, 220 °C, and 240 °C) and brief soaking times ($t_{AA} < 3$ h) were considered in order to promote the industrial applicability of the heat treatment.

DTA was performed to analyze the temperature (190 °C - 240 °C) and soaking time range (0.5 h - 3 h) to identify the optimized AA parameters. At the same time, aging curves, Raman spectroscopy, and XRD analysis were employed to evaluate the effects of thermal exposure on the hardness and the RS of the alloy, and the results were corroborated by microstructural analysis on samples subjected to different thermal exposure levels (0.5 h at 190 °C, 1.5 h at 220 °C, and 3 h at 240 °C). In conclusion, results were used to obtain iso-hardness and iso-RS reduction maps to identify possible solutions for taking advantage of different T_{AA} and t_{AA} conditions.

2. Experimental

2.1. Samples production

Carpenter Additive supplied the commercially available spherical gas atomized powder of the AlSi10Mg alloy, used as feedstock material, with a particle size range of 29.2–73.6 μm. The chemical composition given by the supplier is reported in Table 1.

A low-temperature drying process (3 h at 60 °C) and sieving (in 230 mesh sieves) were performed before the PBF-LB process on the powder to avoid particle adhesion and improve flowability.

All specimens were produced on a SISMA MYSINT100RM, a PBF-LB machine system with a Trumpf fiber laser source, according to the process parameters described in Table 2. The build chamber was filled with inert N_2 gas to reduce the O_2 residual content to 0.1 vol%. Samples were made with a no-heated platform to emphasize the effects of the AA.

The sample dimensions (1 ×40×100 mm^3) were chosen to minimize the thermal stress along x-axis direction (Fig. 1), similar to previous work investigating RS via XRD analysis [34].

2.2. Heat treatments, thermal analysis, and aging curves

Three different temperatures (T_{AA}: 190 °C, 220 °C, 240 °C) and soaking times (t_{AA}: 0.5 h, 1.5 h, 3 h) were investigated. Test conditions were chosen based on both literature works ($T_{AA} > 180$ °C), as previously discussed, and thermal analyses performed on the AB alloy to promote the precipitation of reinforcing phases (precursors of the Mg_2Si) and Si-nanoparticles occurring in the range 150 °C - 250 °C. In particular, thermal analyses were carried out using a differential thermal analyzer (DTA, Rheometric Scientific STA1500), and specimens of about 20 mg were heated in the temperature range from 100 °C to 400 °C with a heating rate of 15 °C min^{-1} under Ar atmosphere. RSI Orchestrator software was used to determine from DTA curves onset, peak temperatures, and enthalpy of transformations. DTA was performed on the AB alloy and heat-treated samples at selected conditions to verify the modifications in the precipitation sequence and kinetics of the second phases after AA. The AA heat treatments were performed in air, using an electric furnace with a temperature control of ± 2 °C. Two K-type thermocouples verified the temperature uniformity during the heat treatment. Aging curves were elaborated using Vickers hardness with 1 kg load (HV1) tests according to ASTM E92–17. An average of at

Table 1
Chemical composition (wt%) of AlSi10Mg feedstock powder supplied by the producer and nominal composition (wt%) of the AlSi10Mg alloy according to EN AC-43000.

Element (wt%)	Al	Si	Mg	Fe	Cu	Mn	Ni	Pb	Sn	Ti	Zn
Powders	Bal.	9.97	0.38	0.11	<0.01	<0.01	<0.01	<0.01	<0.01	0.01	<0.01
EN AC-43000	Bal.	9–11	0.20–0.45	<0.55	<0.05	<0.45	<0.05	<0.05	<0.05	<0.15	<0.10

Table 2
PBF-LB process parameters used for sample production.

Power [W]	Scan speed [mm/s]	Layer thickness [mm]	Hatch spacing [mm/s]	Spot diameter	Energy density [J/mm^3]	Scan strategy
175	800	0.02	0.08	0.055	137	Chessboard 3 mm x 3 mm rotated of 45° between subsequent layers

least five measurements was carried out for each point reported in the aging curves.

2.3. Microstructural investigation

Microstructural analyses were carried out on the AB and heat-treated samples using field emission-gun scanning electron microscopy (TESCAN MIRA3 FEG-SEM) equipped with energy-dispersive X-ray spectroscopy (EDS, Brucker Quantax 200/30 mm^2) and electron backscattered diffraction (EBSD) detector e$^-$Flash HD. Prior to the microstructural investigation, metallographic samples were embedded in conductive resin, polished following standard metallographic procedures up to 1 μm polycrystalline diamond suspension according to ASTM E3–11(2017), and then etched with Keller's reagent (2.5 mL HNO_3, 1.5 mL HCl, 1.0 mL HF and 95 mL distilled water) according to ASTM E407–07(2015)e1. Samples for EBSD analysis were polished down by ion milling with Ar + ions in a SEMPrep2 (model SC2000) device to obtain an optimal surface finish. A step size of 0.5 μm was used for the EBSD maps. MTEX® software was employed for EBSD analysis, using a misorientation angle of 5° to identify low-angle grain boundaries (LAGB) and a misorientation angle of 15° to identify high-angle grain boundaries (HAGB).

2.4. Residual stress analysis

Residual stress in AB and heat-treated samples were evaluated by X-ray diffraction (XRD) analysis and Raman spectroscopy.

Raman is commonly used to assess RS for Si-based products [35–37], and it has already been utilized in the literature for PBF-LB Al-Si alloys [13,38,39]. In particular, this method was used in a previous study to assess Type II residual stress RS in the PBF-LB AlSi7Mg alloy subjected to different post-process heat treatments, including AA and SR [24]. Raman spectroscopy was carried out directly on the surface of samples resulting from the PBF-LB process, with no alteration due to polishing. At least ten spectra per condition were randomly acquired; each spectrum consisted of ten accumulations with a dwell time of 10 s at room conditions. Spectra were recorded using a Renishaw InVia micro-spectrometer equipped with a Leica DMLM microscope using a 50 mW Ar+ laser source (wavelength 514.5 nm).

XRD analyses were carried out using a G.N.R. StressX X-ray diffractometer equipped with a Cr source (Cr $K_\alpha = 0.22897$ nm), a V filter, and a 3 mm diameter collimator, operating at 25 kV and 4.1 mA in χ-scanning configuration. Type I macro residual stress was determined by the sin2ψ method according to UNI EN ISO 15303:2009 through the measurement of Al <311> diffraction peak shift. For each measurement, nine acquisitions were performed in the ψ scanning angle −40° and 40°, with 30 s acquisition time per point. As for Raman spectroscopy, no surface preparation was performed to avoid any residual stress field modification, and only surface measurements were used. Single-axis measurements (two at the same z-height for each sample) were performed along the z-axis (Fig. 1) since previous literature works [17] demonstrated the collinearity between the maximum stress direction and the building direction.

3. Results

3.1. Aging response

DTA analysis was preliminarily performed on the AB alloy (Fig. 2) to identify the artificial aging temperature (T_{AA}) range to induce the precipitation sequence of the strengthening phases Mg_2Si based on a thermal-controlled diffusion mechanism [6]. Starting from the α supersaturated solid solution (SSS), the precipitation of reinforcing phases during aging follows the path described in Equation 1.

$$\alpha(SSS) \rightarrow GP\ zones \rightarrow \beta'' \rightarrow \beta' \rightarrow \beta \quad (1)$$

The SSS in the case of the conventional cast and wrought alloys is obtained after a dedicated solution treatment followed by water quenching; however, the PBF-LB AlSi10Mg alloy in AB condition is characterized by a comparable supersatured α-Al matrix due to the peculiar solidification conditions. Therefore, it is possible to perform AA directly on the AB alloy to induce the precipitation of reinforcing phases.

From the DTA spectrum of the AB alloy, three exothermic peaks were observed and identified by the letters A, B, and C in Fig. 2, with peak temperatures and enthalpy reported in the same figure.

The peak A (approx. 159 °C) is rarely reported in the literature but can be attributed to the formation of the GP zones due to the Mg enrichment of the Si-rich clusters finely dispersed within the α-matrix, which gradually undergo a simultaneous enlargement [40]. As described by Fallah et al. [41], the initial Si-enrichment of the earliest precipitates is due to the affinity of locally strained areas for higher Si

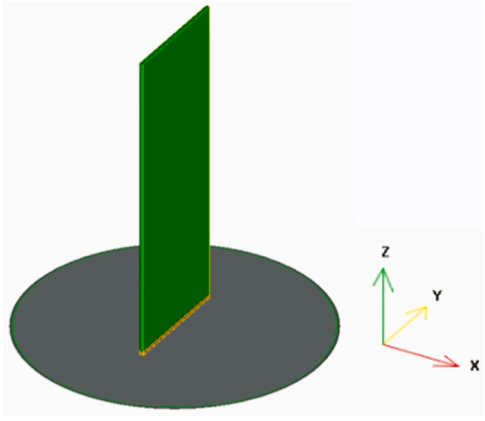

Fig. 1. Sample processed on Materialise Autofab®.

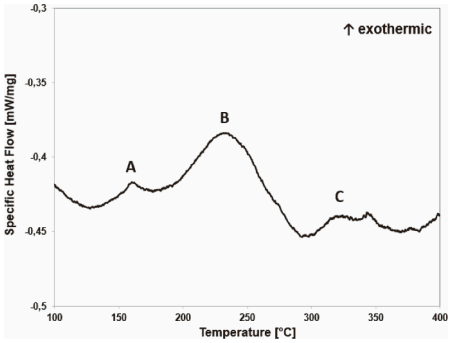

A		B		C	
T peak [°C]	Enthalpy [J/g]	T peak [°C]	Enthalpy [J/g]	T peak [°C]	Enthalpy [J/g]
159	0.4	233	10.8	324	1.9

Fig. 2. DTA spectrum obtained for AB condition and related peak temperatures and enthalpy of A, B, and C exothermic reactions.

concentrations when achieving a metastable equilibrium with the strain-free surrounding matrix. This phenomenon can be promoted using a no-heated platform, which reduces the "in-situ" aging phenomena and promotes a very high Si supersaturation in the Al matrix, showing a peak A more intense than other studies [27,42]. In contrast, the peak B (approx. 233 °C) is broadly discussed in the literature, although at slightly different peak temperatures [17,24,27,30,42]. The specific process parameters used, such as energy density, scanning strategy, and platform temperature, significantly affect the microstructure and supersaturation rate of the AB alloy, shifting the peak temperature of the peak B on the DTA spectrum (Fig. 2). Considering the Si supersaturation in the Al matrix characterizing the AB microstructure, several authors attribute peak B to the precipitation of β" and β' precursor phases [27,29]. In addition, the temperature of peak B is close to the temperature reported for the activation of Si interdiffusion in the Al matrix, which would contribute to the coarsening of the nano-sized Si particles dispersed in the α-Al cells [43,44]. Peak C results as the sum of two signals attributable to different phenomena: (i) the evolution of coherent β" precipitates and semi-coherent β' in stable incoherent β (Mg_2Si) phases [17,42], and (ii) the disaggregation of the eutectic-Si network and consequent formation of the spheroidal Si particles [45].

Peak B is prominent compared to peaks A and C, and it is characterized by a non-negligible enthalpy of transformation (10.8 J/g). The onset peak temperature is approx. 185 °C, and the offset one is approx. 290 °C, with peak temperature located at about 233 °C. Therefore, three different T_{AA} conditions were designed: (i) 190 °C, (ii) 220 °C, and (iii) 240 °C, for an exposure time of up to 3 h. The aim is to take advantage of the maximum strengthening effect from the precipitation of β-Mg_2Si precursor phases occurring in peak B and made possible by the supersaturated solid solution of the AB alloy while avoiding the microstructural coarsening induced by an excessive exposure temperature, which leads to the Si nanoparticle coarsening and the disappearance of the ultrafine cellular structure due to thermal diffusion phenomena.

Aging curves show the hardness evolution for the interested T_{AA} (Fig. 3).

Only the AA at 190 °C was able to strengthen the alloy. The peak-aging condition is reached at 190 °C after only 0.5 h (137 HV1), producing an increase in hardness of 8% compared to the AB condition (127 HV1). Over the peak hardening, the hardness decreases, reaching a value comparable to the AB alloy after 3 h. In contrast, a continuous decrease in hardness is observed at 220 °C and 240 °C. After 3 h, a minimum hardness value equal to 119 HV1 (- 6%) and 111 HV1 (- 13%) is identified for 220 °C and 240 °C curves. These different behaviours can be explained in light of the microstructural evolution undergone by the AB alloy. In particular, three specific T_{AA} and t_{AA} conditions are selected for a more in-depth microstructural characterization: (i) 0.5 h

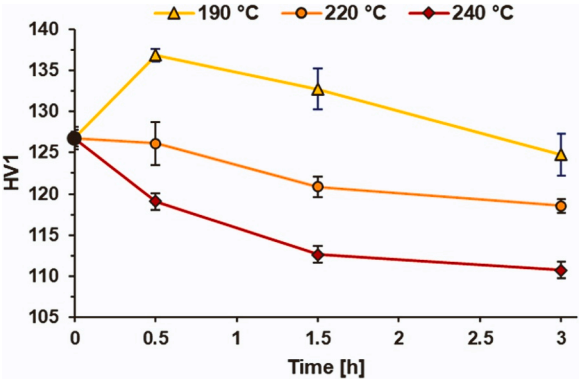

Fig. 3. Aging curves of the PBF-LB AlSi10Mg alloy at 190 °C, 220 °C, and 240 °C. The black point at 0 h identifies AB hardness.

at 190 °C (hereafter AA - 190), i.e., peak aging condition; (ii) 1.5 h at 220 °C (hereafter AA - 220), i.e., a condition of intermediate thermal exposure; (iii) 3 h at 240 °C (hereafter AA - 240), i.e., maximum thermal exposure and lowest hardness condition.

As shown in Figs. 4(a) and (b), the AB alloy is characterized by a microstructure consisting of an ultrafine sub-micrometric structure consisting of supersaturated α-Al cells, in which nanometric Si particles are dispersed, surrounded by a Si-eutectic network. α-Al cells arrange the cusp-like randomized pattern of Melt Pools (MPs) induced by the appropriate scanning strategy used to promote a more isotropic microstructure and high bulk density [46]. However, the layer-to-layer deposition process of the PBF-LB technology introduces inhomogeneous regions, such as Melt Pool Boundaries (MPB) and Heat Affected Zones (HAZ), as the result of the partial re-melting of the previously deposited layers and heating-cooling thermal cycles, respectively. These solidification conditions promote coarser sub-micrometric α-Al cells in the MPB, nearby the eutectic-Si network appears fragmented and small agglomerated Si particles are present in correspondence with HAZ. The α-Al cell sizes and the eutectic-Si network morphology deeply influence the strengthening mechanisms of the PBF-LB AlSi10Mg alloy [9]. However, a marked tendency to evolve towards a more stable condition characterizes the metastable microstructure, which changes its microstructural features after prolonged exposure to high temperatures, as described by the DTA analysis (Fig. 2).

Focusing on heat-treated conditions, at low magnification (Fig. 4(c, e)), AA - 190 and AA - 220 samples show no appreciable changes in the morphology and integrity of the eutectic-Si network compared to the AB sample (Fig. 4(a)). However, a higher density of nanometric Si particles within the α-Al cells than in the AB sample is visible (Fig. 4(d,f)). During the thermal exposure, the Si particles increased in size and density inside the α-Al cells due to the supersatured condition of the Al matrix; in fact, the excess of Si atoms precipitates from the Al matrix and diffuse to minimize the internal energy of the system by forming new Si particles and coarsening pre-existing nano-sized Si particles [47]. In addition, the short diffusion distances of Si and Mg atoms from the supersatured Al lattice in the AB alloy promote the precipitation of the strengthening β-Mg_2Si precursors following thermal exposure [48]. Then, as the intensity of thermal exposure increases (higher T_{AA} or longer t_{AA}), the strengthening precipitates coalesce, passing by intermediate forms, β" and β', to stable incoherent phases β, as confirmed by the aging curves (Fig. 3). Even though TEM analysis would be required to investigate these mechanisms thoroughly, several authors agree that prolonged thermal exposure generates diffusion-driven phenomena and a rapid coarsening of the reinforcing precipitates in heat-treated Al cast alloys [49–51] and heat-treated PBF-LB AlSi10Mg alloy [24,27,47]. These larger precipitates contribute less to alloy strengthening due to (i) a lower precipitate/matrix interface area, (ii) a higher incoherence between strengthening phases and α-Al matrix, and (iii) a lower density of

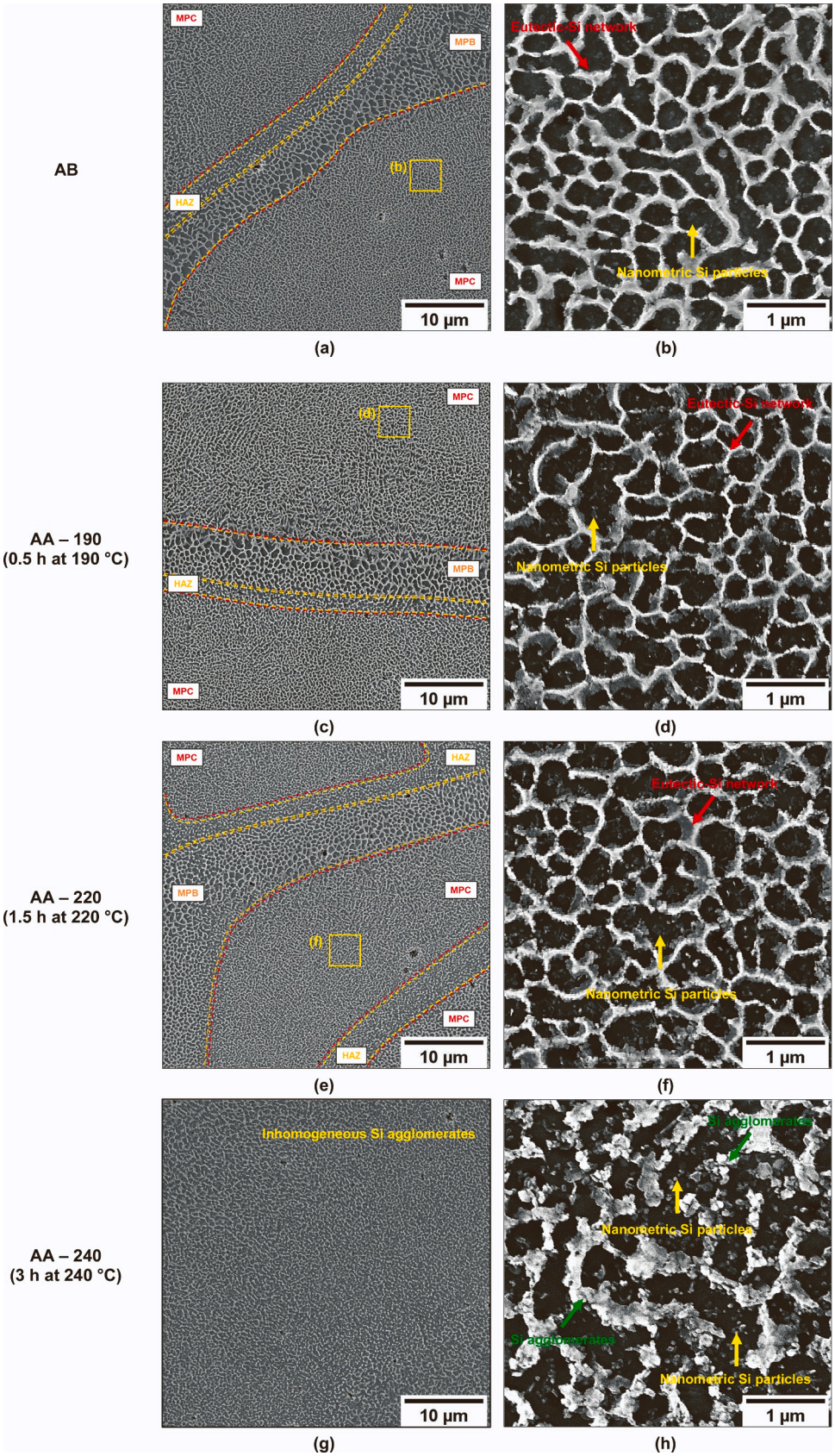

Fig. 4. PBF-LB AlSi10Mg microstructures in different conditions: a) and b) AB; c) and d) AA - 190 (0.5 h at 190 °C); e) and f) AA - 220 (1.5 h at 220 °C); g) and h) AA - 240 (3 h at 240 °C). Red arrows indicate the continuous eutectic-Si network. Yellow arrows highlight nanometric Si particles embedded into the α-Al matrix. Green arrows point out spaced Si agglomerates. The microstructures were analyzed from a section parallel to the printing platform (XY plane in Fig. 1).

obstacles to the dislocation movement.

Since the solid-state atomic diffusion is a time- and temperature-dependent phenomenon, the AA - 240 heat treatment activates more intense diffusion processes and induces evident dimensional and morphological changes in the Si phase. The higher temperature (240 °C) and the longer soaking time (3 h) cause the fragmentation of the eutectic-Si network in correspondence of discontinuities such as joints or necks of the Si branches due to Si atoms diffusion. This process also leads to the coarsening of pre-existing Si particles (Fig. 4(h)). In particular, the formation of large and widely spaced Si agglomerates at the expense of the continuous eutectic-Si network (Fig. 4(h)) is linked to a thermodynamically and energetically spontaneous process that acts to reduce the internal energy of the system (Ostwald ripening phenomenon) through surface self-diffusion and Al-Si interdiffusion [43]. The lamellar Si phase of the eutectic network possesses a large surface-to-volume ratio, which results in high internal energy of the system due to the significant surface energy. On the contrary, the coarser Si agglomerates are characterized by low internal energy due to the more favorable surface-volume ratio. Therefore, the diffusion of Si atoms to form coarser Si agglomerates leads to the fracture and the disappearance of the finer interconnected fibers of the eutectic-Si network, of which remain only small fractions at sub-cell boundaries of the α-Al matrix (Fig. 4(h)).

The irregular Si-rich clusters formed during the AA - 240 heat treatment reduce the strengthening mechanisms, such as microstructural refinement and aggregated second phases. The strengthening phases (Si and Mg_2Si precursors) coarsening, the loss of microstructural refinement, and the partial disintegration of the eutectic-Si network, therefore, contributed to the significant gap (- 26 HV1) between the peak-aged condition (AA - 190) and the lowest hardness condition (AA - 240). In particular, the hardness trend evaluated in Fig. 3 is in line with the microstructural analysis: the microstructural changes lead to a decrease in hardness, which can be explained not only by the phenomenon of overaging but also by the microstructural evolution of the alloy.

As described by [52,53], the high content of Si segregated along α-Al cell boundaries causes residual stress due to the thermal expansion coefficient mismatch between Al and Si. This condition can favor the formation of dislocations in the cell boundaries and, consequently, a different level of dislocation density between MPC and peripheral zones (MPB and HAZ) or inside large columnar grains [54,55], as described by EBSD analysis reported in Fig. 5.

As shown in Fig. 5(a,b), the AA - 240 sample retained the grain texture of the AB condition. Both conditions are characterized by columnar grains oriented along the building direction (z-axis), driven by high thermal gradient and epitaxial growth from the underlying layers [56], and smaller equiaxed grains, which are distributed along the MPBs as a consequence of the partial remelting of the previously solidified layer during the deposition of the upper layer [57]. The Inverse Pole Figures (IPF) and corresponding pole figure maps (Fig. 5(a,b)) indicate the preferential orientation of the columnar grains along the <100> direction (parallel to the build direction, z-axis) as an effect of epitaxial solidification. In contrast, small equiaxed grains along the MPBs were characterized by a non-preferred orientation. As a first result, the AA-240 heat treatment did not induce grain growth (Fig. 5(c,d)), confirming what was reported in [56,58]. However, the KAM (Kernel Average Misorientation) and GOS (Grain Orientation Spread) maps in Fig. 5(c-f)), show some differences between the as-built and heat-treated conditions in terms of local deformation, probably caused by the accumulation of geometrically necessary dislocations [58,59]. The AB alloy exhibits a highly inhomogeneous local misorientation distribution, characterized by an increased density beneath the MPBs of dislocations with a threshold angle lower than LAGB (Fig. 5(e)), resulting from the large thermal gradient between the MPBs and the surrounding areas which triggered local plastic deformations within the columnar grains [59]. Furthermore, the columnar grains are characterized by a high variation in GOS values, indicating a high amount of local strains due to the epitaxial growth mechanism that occurred during solidification (Fig. 5(g)). On the contrary, equiaxed grains, formed due to the remelting process of the underlying layer, are characterized by an extremely low GOS value [55]. Aging at 240°C for 3 hours appeared to have a limited effect in reducing localized disorientation within the columnar grain and in the regions close to the MPBs (Fig. 5(f)); however, the relative GOS map (Fig. 5(g)) indicates a more uniform distribution of grain misorientation, implying that a partial recovery process as occurred due to the reorganization of the lattice defects according to a configuration with lower energy content, characterized by the formation of dislocation walls, thus reducing the Type III RS.

The DTA analysis was repeated on heat-treated samples (AA - 190, AA - 220, and AA - 240) to evaluate the residual potential of the Mg_2Si phase precipitation sequence and of the Si atom diffusion that led to the disaggregation of the eutectic-Si network (Peaks B and C) (Fig. 6)

The DTA curves of the heat-treated samples confirm the microstructural evolution in the AB alloy after direct aging.

Peak B of the AA - 190 condition is shifted at higher temperatures and its transformation enthalpy is equal to 2.4 J/g, lower than in the AB condition; this agrees with the fact that after AA - 190 treatment, only the formation of the semicoherent β' phase took place. On the contrary, peak B is no longer identifiable in the samples after AA - 220 and AA - 240 heat treatment (Fig. 6) because the precipitation sequence of Mg_2Si precursor phases occurred entirely before the DTA test, confirming what was observed from the aging curves (Fig. 3). In this way, the rearrangement of β-phase would contribute only to the enthalpy transformation of the peak C [17,42].

The enthalpy associated with peak C (rearrangement of stable incoherent β (Mg_2Si) phases and dissolution of the eutectic-Si network) is slightly higher in AB, AA - 190, and AA - 220 conditions (1.9 J/g, 2.2 J/g, and 2.3 J/g, respectively) than in the AA - 240 one (1.4 J/g). This could depend on the evolution stage of the Si-eutectic network towards a more stable condition (Fig. 4), which influences the characteristics of the peak C signal [17,24,27]. Therefore, the AB, AA - 190, and AA - 220 conditions, starting from a continuous eutectic-Si network still to be dissolved, are characterized by an enthalpy associated with peak C slightly higher than the AA – 240 condition which starts from a fragmented eutectic-Si network (Fig. 4(h)), where the formation of the first Si aggregates is visible. However, the AA - 240 condition is only in the early stage of microstructural evolution, thus affecting the enthalpy of the C peak to a limited extent. As described by [17,24,27] in fact, the enthalpic peak associated with the Si diffusion mechanism of the PBF-LB AlSi10Mg alloy (Peak C in this study) becomes substantially flat only for those heat-treated samples where the transition from the eutectic-Si network to spheroidal Si particles is occurred completely (thermal exposure from approximately 300 °C and above). Furthermore, the rearrangement of the stable incoherent β-phase possibly contributes to an increase in the enthalpy of the peak C for all the analyzed conditions, without therefore introducing further differences in the single enthalpy values.

3.2. Residual stress analysis

As described by EBSD analysis in Section 3.1, sufficiently high artificial aging temperatures (3 h at 240 °C) can be able to induce partial recovery and promote a dislocation rearrangement able to relieve Type III RS. However, thermal exposure (190 °C, 220 °C, and 240 °C for up to 3 hours) also affects Type II RS and Type I RS, which were evaluated via Raman analysis and XRD analysis.

Raman spectroscopy is based on the characterization of the Raman Si shift by evaluating the difference in the shift position related to unstressed Si (set at 520 cm^{-1} [13,24]), thus allowing comparison of the Type II RS (intergranular RS due to the presence of different phases and local microstructural inhomogeneities) of the different conditions analyzed. In particular, if the peak is moved to values lower than 520 cm^{-1}, RS is tensile; otherwise, RS is compressive. Raman spectroscopy was performed on the AB alloy, used as a reference, and after

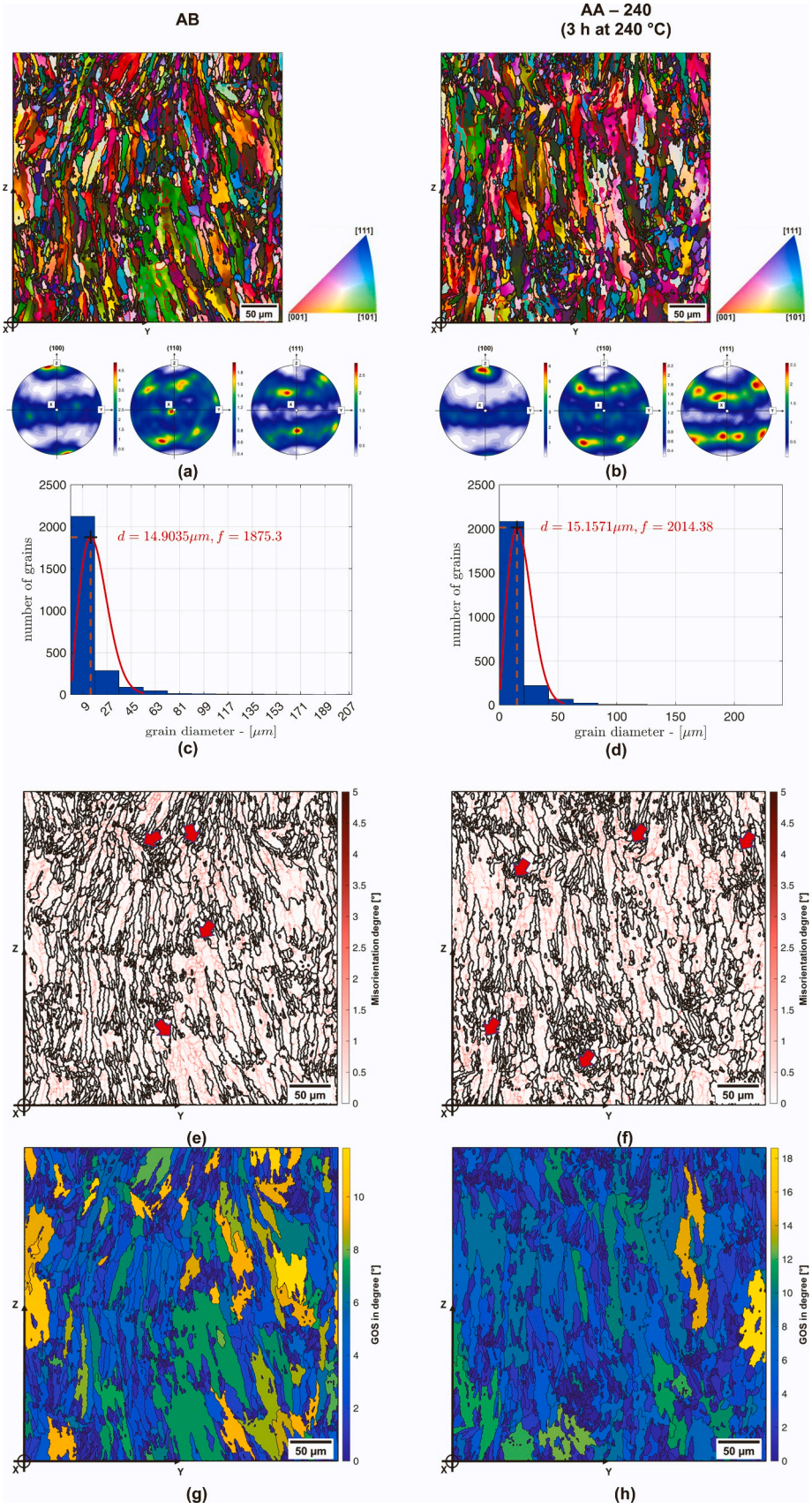

Fig. 5. Inverse pole-figure (IPF) maps and corresponding (100), (110), and (111) pole figures (a,b), histograms of grain diameter (c,d), Kernel Average Misorientation maps (e,f), and Grain Orientation Spread (GOS) maps (g,h) analyzed from plane parallel to building direction (z-axis) for: AB alloy (a,c,e,g), and AA-240 (b,d,f,h) alloy. In IPF maps, red lines indicate LAGB and black lines indicate HAGB. Red arrows indicate an increase in local plastic deformations near the MPBs.

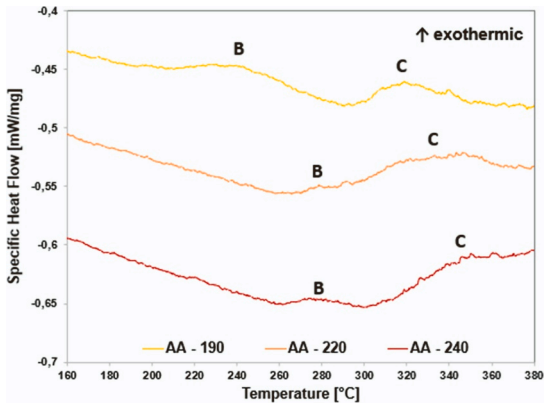

Peak	B		C	
	T peak [°C]	Enthalpy [J/g]	T peak [°C]	Enthalpy [J/g]
AB	233	10.8	324	1.9
AA – 190	259	2.4	320	2.2
AA – 220	280	0.2	334	2.3
AA – 240	278	0.4	345	1.4

Fig. 6. DTA spectrum of (i) AA - 190 (0.5 h at 190 °C), (ii) AA - 220 (1.5 h at 220 °C), and (iii) AA - 240 (3 h at 240 °C) conditions, and related peak temperatures and enthalpy of B, and C exothermic reactions, which are also reported for the AB condition.

exposition at 190 °C, 220 °C, and 240 °C up to 3 h to determine the effect of the thermal exposure on the micro-stress acting on the fine Si precipitates. Regarding Si-peak shift (average values and standard deviations), results are reported in Fig. 7 as a function of temperature and soaking time and compared to the reference value for the un-stressed Si.

Based on Raman results, the AB alloy is characterized by tensile Type II RS (Raman shift about 514 cm^{-1}). Thermal exposure at high temperatures (220 °C and 240 °C) decreased RS, even if complete relief was not achieved. Considering standard deviations, Raman shifts are comparable and approximately equal to 516 cm^{-1} On the other hand, RS were little affected by the exposure at 190 °C. In fact, if standard deviations are considered, the Si shift is close to the AB condition regardless of soaking time. Therefore, these results show that stress relief is more affected by heat treatment temperature rather than soaking time.

As expected, a higher thermal exposure promotes a higher RS relief. This phenomenon is related to two different causes. With prolonged holding at high temperatures, the thermal-controlled diffusion mechanisms dissolve the eutectic-Si network into numerous irregular Si-rich clusters until forming coarser and more distanced Si particles [47]. The microstructural rearrangement reduces the local stress inhomogeneities induced by sequential heating-cooling cycles during printing, and the localized shear stress at the Al cell/Si network interface, promoting higher cohesion between Si and Al phases [32,52,60]. Furthermore, according to Maeshima et al. [53], the high content of Si atoms, which are characterized by a lower atomic radius than Al (0.118 nm for Si and 0.143 nm for Al, respectively), in the Al lattice causes a lattice deformation in AB alloy and promotes the development of RS. Therefore, reducing Si in solid solution by exposure to high temperature promotes RS relief, as described by Raman analysis

Fig. 8 reports the variation in Type I RS (macroscopic RS equal to the component size scale) measured by XRD analysis along the building direction (z-axis) on the surface of the PBF-LB AlSi10Mg alloy after AA heat treatment at 190 °C, 220 °C, and 240 °C up to 3 h, focusing on the macro-stress acting on the Al matrix.

The AB specimens have an average value of the superficial residual stress (σ_{RS}) equal to 114 ± 26 MPa. This value is comparable to the ones reported in [17,61], and it should be considered that it represents about 50% of the yield strength of the PBF-LB AlSi10Mg alloy (according to data reported in the literature [20,30,36]). In particular, RS mainly affect high-cycle fatigue strength, by adding themselves to the cyclic load applied and, therefore, by increasing the level of stress suffered by the material and by acting as promoters for crack nucleation and growth [62] Considering that for the PBF-LB AlSi10Mg alloy the killer defects, such as gas pores or lacks of fusion, are generally localized either at the surface or in the substrate [61,63], it is evident how the superficial tensile residual stress is able to negatively affect the fatigue performances of the PBF-LB AlSi10Mg alloy and need to be reduced.

AA significantly relieved the tensile σ_{RS} resulting from the PBF-LB printing. In particular, the superficial tensile σ_{RS} measured on the heat-treated samples is lower than AB one in all analyzed conditions, with a minimum evaluated after 3 h at 240 °C equal to 37 ± 24 MPa. However, it is worth noticing that the lowest thermal exposure condition (0.5 h at 190 °C) also shows a significant decrease in σ_{RS}, achieving a value equal to 74 ± 11 MPa.

The decrease in Type I RS can be attributed to the softening of the AlSi10Mg alloy at high temperatures, which promotes the recovery of the RS caused by the differential contraction-expansion of the material during the heating and cooling cycles of the PBF-LB process [60]. Therefore, greater thermal exposure favors a higher relief of RS. Furthermore, a more significant microstructural rearrangement induced by more severe heat treatments, as occurred in the AA - 240 condition (Fig. 4), may cause a further reduction in Type I RS by decreasing the stress-strain states across the interface between the Al and Si phases [30,52].

3.3. Heat treatment design

Based on previous analysis, iso-hardness and iso-RS reduction maps, obtained by aging curves and XRD analysis data, are elaborated to identify the possible effects of different T_{AA} and t_{AA} conditions on the mechanical hardness of the heat-treated alloy (Fig. 9).

As expected, increasing, or lowering the thermal exposure level to

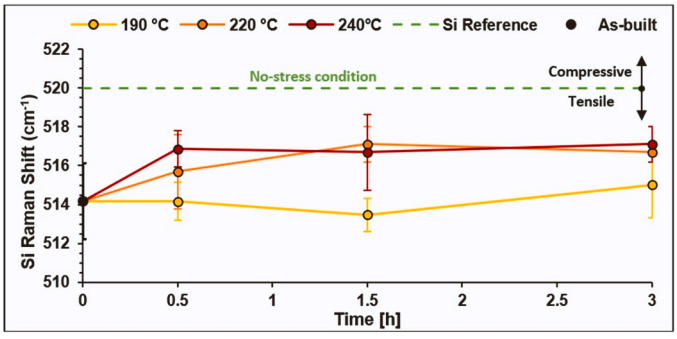

Fig. 7. Si peak shift of AB and heat-treated samples at 190 °C, 220 °C, and 240 °C, evaluated via Raman spectroscopy.

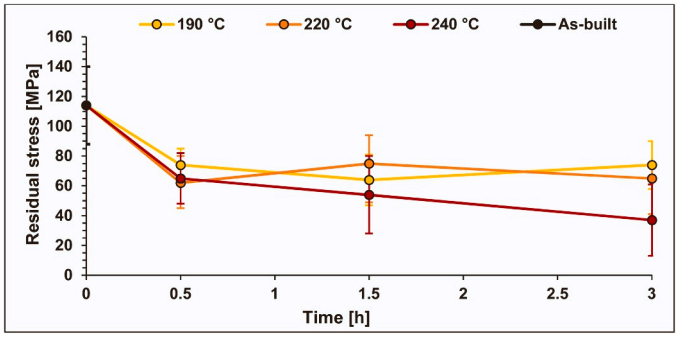

Fig. 8. Tensile residual stress measured on AB and heat-treated samples at 190 °C, 220 °C, and 240 °C by XRD analysis.

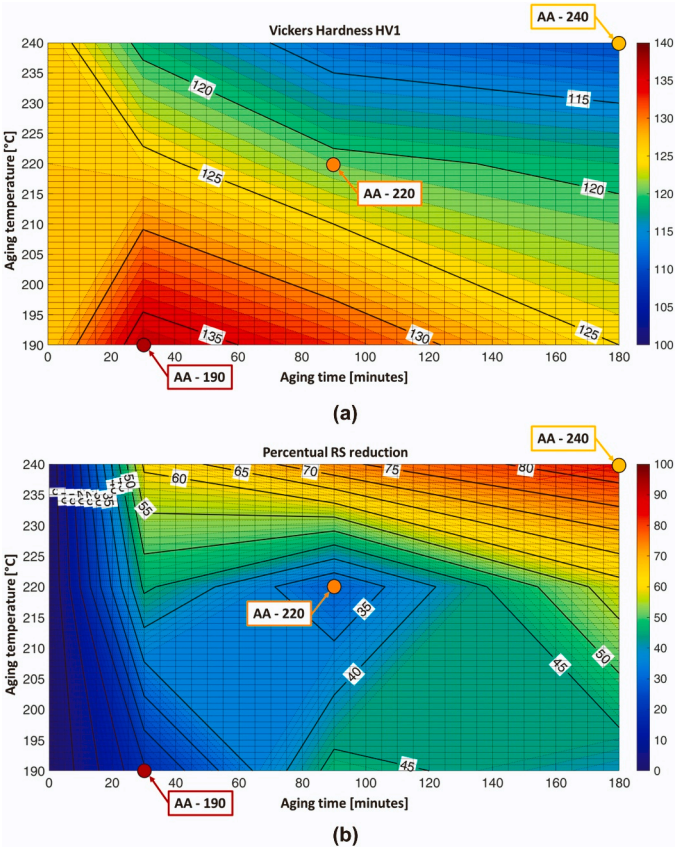

Fig. 9. Iso-hardness (a) and iso-RS reduction (b) maps for a temperature range of 190 °C - 240 °C and soaking time up to 3 h.

which PBF-LB AlSi10Mg alloy is subjected leads to significant changes in hardness-residual stress trade-off. It is interesting to evaluate how the simultaneous achievement of the peak-hardening conditions and the maximum RS relief appears impossible. However, these maps allow to identify the heat treatment conditions to obtain target values of hardness and/or residual stresses. This result assumes a significant industrial value to predict the possible mechanical performances after heat treatment of the components according to the service conditions.

The literature seems to fit data developed by iso-hardness and iso-RS reduction maps elaborated in the present work. For example, data reported by Fiocchi et al. [17] are well aligned: (i) AA consisting of 180 minutes at 244 °C induces a decrease in RS of 80% and a hardness value equal to 105 HV, in line with the data reported in the top corner on the right in Fig. 9; (ii) AA consisting of 170 °C for 90 min leads to a decrease in RS by 35% and an increase in hardness up to 145 HV, in line with what is observed in the lower part of the graphs shown in Fig. 9. These results support hardness and RS trends reported in Fig. 9, considering the different process parameters and printing systems used to produce the specimens. In particular, although it is really difficult to obtain a predictive model considering all the parameters and the various printing systems in play, the trends of hardness and RS here reported represent a valid tool for a first evaluation of changes occurring as a function of temperatures and soaking time.

4. Conclusion

The present work aims to define a method for the identification of direct artificial aging (AA) parameters that enhance the trade-off between hardness and residual stress relief of the PBF-LB AlSi10Mg alloy produced with no heated platform. Based on thermal analysis, aging curves were performed at 190 °C, 220 °C, and 240 °C to evaluate the effects on the mechanical performance of the alloy. Subsequently, microstructural modifications induced by different thermal exposure conditions (0.5 h at 190 °C (AA - 190), 1.5 h at 220 °C (AA - 220), and 3 h at 240 °C (AA - 240)) were analyzed. Finally, relieving of residual stress obtainable by AA heat treatment was evaluated by Raman and XRD analysis. Results can be synthesized as follows:

- Hardness shows a slight increase (+ 8%) in AA - 190 condition compared to the AB alloy (127 HV1), which is promoted by a greater contribution of precipitation hardening (Mg_2Si precursor phases) and the maintenance of the various strengthening mechanisms (solid solution, microstructural refinement, and aggregate second phases) that characterizes the PBF-LB AlSi10Mg alloy. After AA at higher temperatures (220 °C and 240 °C), the hardness decreases up to a maximum of 13% (111 HV1) in the AA – 240 condition due to the coarsening of the strengthening precipitates and formation of large and widely spaced Si agglomerates. EBSD analysis shows a partial recovery process for AA - 240 condition due to the reorganization of the lattice defects and the formation of dislocation walls within the grain structure.
- Raman and XRD analyses show comparable trends in residual stress relief. In particular, the Raman analysis highlights a decrease in Type II RS with increasing thermal exposure, due to reduction of both Al matrix supersaturation and local stress inhomogeneities at the Al soft-phase/Si hard-phase interface. At the same time, XRD analysis shows a temperature- and soaking time-dependent relief effect of the Type I RS due to increased material softening and more significant microstructural rearrangement. At low temperature and soaking time (AA – 190 condition), the Type I RS value decreases by 35% with respect to the AB alloy, while, as the thermal exposure increases (AA - 240 condition), the RS value decreases by 68%.

The results described by the elaborated iso-hardness and iso-RS relief indicate the possibility of designing artificial aging to optimally balance the contribution of the strengthening mechanisms and residual stress relief on the mechanical performance of the PBF-LB AlSi10Mg alloy. This outcome is extremely important considering the wide industrial use of structural components in Al-Si-Mg alloys, which could benefit from specific customization of the mechanical performance by artificial aging treatment.

Declaration of Competing Interest

The authors declare that they have no known competing financial interests or personal relationships that could have appeared to influence the work reported in this paper.

Acknowledgments and Funding Information

Financed by the European Union-NextGenerationEU (National Sustainable Mobility Center CN00000023, Italian Ministry of University and Research Decree n. 1033–17/06/2022, Spoke 11-Innovative Materials & Lightweighting), and National Recovery and Resilience Plan (NRRP), Mission 04 Component 2 Investment 1.5-NextGenerationEU, Call for tender n. 3277 dated 30 December 2021. The opinions expressed are those of the authors only and should not be considered representative of the European Union or the European Commission's official position. Neither the European Union nor the European Commission can be held responsible for them.

The authors gratefully acknowledge Simone Di Piazza and Simone Messieri (Ducati Motor Holding S.p.A) for fruitful collaboration regarding potential applications of the results in the transport field.

References

[1] S. Chowdhury, N. Yadaiah, C. Prakash, S. Ramakrishna, S. Dixit, L.R. Gupta, D. Buddhi, Laser powder bed fusion: a state-of-the-art review of the technology, materials, properties & defects, and numerical modelling, J. Mater. Res. Technol. 20 (2022) 2109–2172, https://doi.org/10.1016/j.jmrt.2022.07.121.

[2] A. Khorasani, I. Gibson, J.K. Veetil, J.K, A.H. Ghasemi, A review of technological improvements in laser-based powder bed fusion of metal printers, Int. J. Adv. Manuf. Technol. 108 (2020) 191–209, https://doi.org/10.1007/s00170-020-05361-3.

[3] H.R. Kotadia, G. Gibbons, A. Das, P.D. Howes, A review of laser powder bed fusion additive manufacturing of aluminium alloys: microstructure and properties, Addit. Manuf. 46 (2021) 102155, https://doi.org/10.1016/j.addma.2021.102155.

[4] S.C. Altıparmak, V.A. Yardley, Z. Shi, J. Lin, Challenges in additive manufacturing of high-strength aluminium alloys and current developments in hybrid additive manufacturing, Int. J. Lightweight Mater. Manuf. 4 (2) (2021) 246–261, https://doi.org/10.1016/j.ijlmm.2020.12.004.

[5] L. Zhao, L. Song, J.G. Santos Macías, Y. Zhu, M. Huang, A. Simar, Z. Li, Review on the correlation between microstructure and mechanical performance for laser powder bed fusion AlSi10Mg, Addit. Manuf. 56 (2022) 102914, https://doi.org/10.1016/j.addma.2022.102914.

[6] J. Fite, S.E. Prameela, J.A. Slotwinski, T.P. Weihs, Evolution of the microstructure and mechanical properties of additively manufactured AlSi10Mg during room temperature holds and low temperature aging, Addit. Manuf. 36 (2020) 101429, https://doi.org/10.1016/j.addma.2020.101429.

[7] A. Mertens, J. Delahaye, O. Dedry, B. Vertruyen, J.T. Tchuindjang, A.M. Habraken, Microstructure and Properties of SLM AlSi10Mg: understanding the Influence of the Local Thermal History, Procedia Manuf. 47 (2020) 1089–1095, https://doi.org/10.1016/j.promfg.2020.04.121.

[8] W. Li, S. Li, J. Liu, A. Zhang, Y. Zhou, Q. Wei, C. Yan, Y. Shi, Effect of heat treatment on AlSi10Mg alloy fabricated by selective laser melting: microstructure evolution, mechanical properties and fracture mechanism, Mater. Sci. Eng. A. 663 (2016) 116–125, https://doi.org/10.1016/j.msea.2016.03.088.

[9] N. Takata, M. Liu, H. Kodaira, A. Suzuki, M. Kobashi, Anomalous strengthening by supersaturated solid solutions of selectively laser melted Al–Si-based alloys, Addit. Manuf. 33 (2020) 101152, https://doi.org/10.1016/j.addma.2020.101152.

[10] J.L. Bartlett, X. Li, An overview of residual stresses in metal powder bed fusion, Addit. Manuf. 27 (2019) 131–149, https://doi.org/10.1016/j.addma.2019.02.020.

[11] A. Salmi, E. Atzeni, History of residual stresses during the production phases of AlSi10Mg parts processed by powder bed additive manufacturing technology, Virtual Phys. Prototyp. 12 (2) (2017) 153–160, https://doi.org/10.1080/17452759.2017.1310439.

[12] S. Marola, D. Manfredi, G. Fiore, M.G. Poletti, M. Lombardi, P. Fino, L. Battezzati, A comparison of selective laser melting with bulk rapid solidification of AlSi10Mg alloy, J. Alloy. Compd. 742 (2018) 271–279, https://doi.org/10.1016/j.jallcom.2018.01.309.

[13] S. Marola, S. Bosia, A. Veltro, G. Fiore, D. Manfredi, M. Lombardi, G. Amato, M. Baricco, L. Battezzati, Residual stresses in additively manufactured AlSi10Mg: Raman spectroscopy and X-ray diffraction analysis, Mater. Des. 202 (2021) 109550, https://doi.org/10.1016/j.matdes.2021.109550.

[14] Y. Chen, H. Sun, Z. Li, Y. Wu, Y. Xiao, Z. Chen, S. Zhong, H. Wang, Strategy of residual stress determination on selective laser melted Al alloy using XRD, Materials 13 (2020) 451, https://doi.org/10.3390/ma13020451.

[15] G. Yu, D. Gu, D. Dai, M. Xia, C. Ma, Q. Shi, On the role of processing parameters in thermal behavior, surface morphology and accuracy during laser 3D printing of aluminum alloy, J. Phys. D: J. Phys. D: Appl. Phys. 49 (2016) 135501, https://doi.org/10.1088/0022-3727/49/13/135501.

[16] J.H. Rao, Y. Zhang, K. Zhang, X. Wu, A. Huang, Selective laser melted Al-7Si-0.6Mg alloy with in-situ precipitation via platform heating for residual strain removal, Mater. Des. 182 (2019) 108005, https://doi.org/10.1016/j.matdes.2019.108005.

[17] J. Fiocchi, C.A. Biffi, C. Colombo, C, L.M. Vergani, A. Tuissi, Ad Hoc heat treatments for selective laser melted alsi10mg alloy aimed at stress-relief and enhancing mechanical performances, JOM 72 (2020) 1118–1127, https://doi.org/10.1007/s11837-019-03973-z.

[18] L. Wang, X. Jiang, Y. Zhu, Z. Ding, X. Zhu, J. Sun, B. Yan, Investigation of performance and residual stress generation of AlSi10Mg processed by selective laser melting, Adv. Mater. Sci. Eng. 2018 (2018) 1–12, https://doi.org/10.1155/2018/7814039.

[19] E. Cerri, E. Ghio, G. Bolelli, Effect of the distance from build platform and post-heat treatment of AlSi10Mg alloy manufactured by single- and multi-laser selective laser melting, J. Mater. Eng. Perform. 30 (2021) 4981–4992, https://doi.org/10.1007/s11665-021-05577-8.

[20] R. Casati, M. Hamidi Nasab, M. Coduri, V. Tirelli, M. Vedani, Effects of platform pre-heating and thermal-treatment strategies on properties of AlSi10Mg alloy processed by selective laser melting, Metals 8 (2018) 954, https://doi.org/10.3390/met8110954.

[21] D. Buchbinder, W. Meiners, K. Wissenbach, R. Poprawe, Selective laser melting of aluminum die-cast alloy – correlations between process parameters, solidification conditions, and resulting mechanical properties, J. Laser Appl. 27 (2015) S29205, https://doi.org/10.2351/1.4906389.

[22] A. Sola, A. Nouri, Microstructural porosity in additive manufacturing: the formation and detection of pores in metal parts fabricated by powder bed fusion, J. Adv. Manuf. Technol. (2019) e10021, https://doi.org/10.1002/amp2.10021.

[23] B. Amir, E. Grinberg, Y. Gale, O. Sadot, S. Samuha, Influences of platform heating and post-processing stress relief treatment on the mechanical properties and microstructure of selective-laser-melted AlSi10Mg alloys, Mater. Sci. Eng. A. 822 (2021) 141612, https://doi.org/10.1016/j.msea.2021.141612.

[24] L. Tonelli, E. Liverani, A. Morri, L. Ceschini, Role of direct aging and solution treatment on hardness, microstructure and residual stress of the A357 (AlSi7Mg0.6) alloy produced by powder bed fusion, Met. Mater. Trans. B 52 (2021) 2484–2496, https://doi.org/10.1007/s11663-021-02179-6.

[25] I. Rosenthal, R. Shneck, A. Stern, Heat treatment effect on the mechanical properties and fracture mechanism in AlSi10Mg fabricated by additive manufacturing selective laser melting process, Mater. Sci. Eng. A. 729 (2018) 310–322, https://doi.org/10.1016/j.msea.2018.05.074.

[26] M. Fousová, D. Dvorský, A. Michalcová, D. Vojtěch, Changes in the microstructure and mechanical properties of additively manufactured AlSi10Mg alloy after exposure to elevated temperatures, Mater. Charact. 137 (119-126) (2018) 1044–5803, https://doi.org/10.1016/j.matchar.2018.01.028.

[27] E. Padovano, C. Badini, A. Pantarelli, F. Gili, F. D'Aiuto, A comparative study of the effects of thermal treatments on AlSi10Mg produced by laser powder bed fusion, J. Alloy. Compd. 831 (2020) 154822, https://doi.org/10.1016/j.jallcom.2020.154822.

[28] K.G. Prashanth, S. Scudino, H.J. Klauss, K.B. Surreddi, L. Löber, Z. Wang, A. K. Chaubey, U. Kühn, J. Eckert, Microstructure and mechanical properties of Al–12Si produced by selective laser melting: Effect of heat treatment, Mater. Sci. Eng. A. 590 (2014) 153–160, https://doi.org/10.1016/j.msea.2013.10.023.

[29] V.J. Matjeke, C. Moopanar, A.S. Bolokang, A.S, J.W. van der Merwe, Effect of heat treatment time on the microstructure and mechanical deformation behavior of additive-manufactured AlSi10Mg components, Prog. Addit. Manuf. 5 (2020) 379–385, https://doi.org/10.1007/s40964-020-00139-1.

[30] J. Fiocchi, A. Tuissi, P. Bassani, C.A. Biffi, Low temperature annealing dedicated to AlSi10Mg selective laser melting products, J. Alloy. Compd. 695 (2017) 3402–3409, https://doi.org/10.1016/j.jallcom.2016.12.019.

[31] M. Tocci, A. Pola, M. Gelfi, G.M. La Vecchia, Effect of a new high-pressure heat treatment on additively manufacturedAlSi10Mg alloy, Metall. Mater. Trans. A 51 (2020) 4799–4811, https://doi.org/10.1007/s11661-020-05905-y.

[32] T.H. Park, M.S. Baek, H. Hyer, Y. Sohn, K.A. Lee, Effect of direct aging on the microstructure and tensile properties of AlSi10Mg alloy manufactured by selective laser melting process, Mater. Charact. 176 (2021) 111113, https://doi.org/10.1016/j.matchar.2021.111113.

[33] G. Di Egidio, L. Ceschini, A. Morri, C. Martini, M. Merlin, A novel T6 rapid heat treatment for AlSi10Mg alloy produced by laser-based powder bed fusion: comparison with T5 and conventional T6 heat treatments, Metall. Mater. Trans. B 53 (2022) 284–303, https://doi.org/10.1007/s11663-021-02365-6.

[34] C. Colombo, C. A.Biffi, J. Fiocchi, A. Tuissi, L. Vergani, Effect of optimized heat treatments on the tensile behavior and residual stresses of selective laser melted AlSi10Mg samples, KEM 9 (813) (2019) 364, https://doi.org/10.4028/www.scientific.net/kem.813.364.

[35] T. Menold, E. Hadjixenophontos, R. Lawitzki, G. Schmitz, M. Ametowobla, Crystal defects in monocrystalline silicon induced by spot laser melting, J. Appl. Phys. 127 (2020) 093102, https://doi.org/10.1063/1.5142676.

[36] C. Song, L. Du, L. Qi, Y. Li, X. Li, Y. Li, Residual stress measurement in a metal microdevice by micro Raman spectroscopy, J. Micromech. Microeng. 27 (2017) 105014, https://doi.org/10.1088/1361-6439/aa8912.

[37] B. Matthey, T. Pirling, M. Herrmann, J. Schreiber, Determination of bulk residual stresses in superhard diamond-SiC materials, J. Eur. Ceram. Soc. 40 (2020) 1035–1042, https://doi.org/10.1016/j.jeurceramsoc.2019.11.055.

[38] J.H. Rao, Y. Zhang, X. Fang, Y. Chen, X. Wu, C.H.J. Davies, The origins for tensile properties of selective laser melted aluminium alloy A357, Addit. Manuf. 17 (2017) 113–122, https://doi.org/10.1016/j.addma.2017.08.007.

[39] M. Wang, B. Song, Q. Wei, Y. Zhang, Y. Shi, Effects of annealing on the microstructure and mechanical properties of selective laser melted AlSi7Mg alloy, Mater. Sci. Eng. A vol. 739 (2019) 463–472, https://doi.org/10.1016/j.msea.2018.10.047.

[40] Y. Birol, The effect of homogenization practice on the microstructure of AA6063 billets, J. Mater. Process. Technol. 148 (2) (2004) 250–258, https://doi.org/10.1016/j.jmatprotec.2004.01.056.

[41] L. Girelli, M. Tocci, M. Gelfi, A. Pola, A. Study of heat treatment parameters for additively manufactured AlSi10Mg in comparison with corresponding cast alloy, Mater. Sci. Eng. A 739 (2019) 317–328, https://doi.org/10.1016/j.msea.2018.10.026.

[42] V. Fallah, B. Langelier, N. Ofori-Opoku, B. Raeisinia, N. Provatas, S. Esmaeili, Cluster evolution mechanisms during aging in Al–Mg–Si alloys, Acta Mater. 103 (2016) 290–300, https://doi.org/10.1016/j.actamat.2015.09.027.

[43] D. Lehmhus, T. Rahn, A. Struss, P. Gromzig, T. Wischeropp, H. Becker, High-temperature mechanical properties of stress-relieved AlSi10Mg produced via laser powder bed fusion, additive manufacturing, Materials 15 (2022) 7386, https://doi.org/10.3390/ma15207386.

[44] M. Albu, R. Krisper, J. Lammer, G. Kothleitner, J. Fiocchi, P. Bassani, Microstructure evolution during in-situ heating of AlSi10Mg alloy powders and additive manufactured parts, Addit. Manuf. 36 (2020) 101605, https://doi.org/10.1016/j.addma.2020.101605.

[45] M. Rafieazad, M. Mohammadi, A.M. Nasiri, On microstructure and early stage corrosion performance of heat treated direct metal laser sintered AlSi10Mg, Addit. Manuf. 28 (2019) 107–119, https://doi.org/10.1016/j.addma.2019.04.023.

[46] G. Di Egidio, C. Martini, J. Börjesson, E. Ghassemali, L. Ceschini, A. Morri, Dry sliding behavior of AlSi10Mg alloy produced by Laser-based Powder Bed Fusion: influence of heat treatment and microstructure, Wear 516–517 (2023) 204602, https://doi.org/10.1016/j.wear.2022.204602.

[47] F. Alghamdi, M. Haghshenas, Microstructural and small-scale characterization of additive manufactured AlSi10Mg alloy, SN Appl. Sci. 1 (2019) 255, https://doi.org/10.1007/s42452-019-0270-5.
[48] L. Zhou, A. Mehta, E. Schulz, B. McWilliams, K. Cho, Y. Sohn, Microstructure, precipitates and hardness of selectively laser melted AlSi10Mg alloy before and after heat treatment, Mater. Charact. 143 (2018) 5–17, https://doi.org/10.1016/j.matchar.2018.04.022.
[49] L. Ceschini, A. Morri, S. Toschi, S. Seifeddine, Room and high temperature fatigue behaviour of the A354 and C355 (Al–Si–Cu–Mg) alloys: role of microstructure and heat treatment, Mater. Sci. Eng. A 653 (2016) 129–138, https://doi.org/10.1016/j.msea.2015.12.015.
[50] A. Morri, L. Ceschini, S. Messieri, E. Cerri, S. Toschi, Mo Addition to the A354 (Al–Si–Cu–Mg) casting alloy: effects on microstructure and mechanical properties at room and high temperature, Metals 8 (6) (2018) 393, https://doi.org/10.3390/met8060393.
[51] L. Ceschini, S. Messieri, A. Morri, S. Seifeddine, S. Toschi, M. Zamani, Effect of Cu addition on overaging behaviour, room and high temperature tensile and fatigue properties of A357 alloy, T. Nonferr. Metal. Soc. 30 (11) (2020) 2861, https://doi.org/10.1016/S1003-6326(20)65427-9.
[52] D.K. Kim, J.H. Hwang, E.Y. Kim, Y.U. Heo, W. Woo, S.H. Choi, Evaluation of the stress-strain relationship of constituent phases in AlSi10Mg alloy produced by selective laser melting using crystal plasticity FEM, J. Alloy. Compd. 714 (2017) 687–697, https://doi.org/10.1016/j.jallcom.2017.04.264.
[53] T. Maeshima, K. Oh-ishi, Solute clustering and supersaturated solid solution of AlSi10Mg alloy fabricated by selective laser melting, Heliyon 5 (2) (2019) e01186, https://doi.org/10.1016/j.heliyon.2019.e01186.
[54] H. Qin, V. Fallah, Q. Dong, M. Brochu, M.R. Daymond, M. Gallerneault, Solidification pattern, microstructure and texture development in Laser Powder Bed Fusion (LPBF) of Al10SiMg alloy, Mater. Charact. 145 (2018) 29–38, https://doi.org/10.1016/j.matchar.2018.08.025.
[55] B. Rozegari Ghashghay, H.R. Abedi, S.G. Shabestari, On the capability of grain refinement during selective laser melting of AlSi10Mg alloy, J. Mater. Res. Technol. 24 (2023) 9722–9730, https://doi.org/10.1016/j.jmrt.2023.05.122.
[56] S. Chen, Q. Tan, W. Gao, G. Wu, J. Fan, Z. Feng, T. Huang, A.W. Godfrey, M. Zhang, X. Huang, Effect of heat treatment on the anisotropy in mechanical properties of selective laser melted AlSi10Mg, Mater. Sci. Eng. A. 858 (2022) 144130, https://doi.org/10.1016/j.msea.2022.144130.
[57] F. Alghamdi, X. Song, A. Hadadzadeh, B. Shalchi-Amirkhiz, M. Mohammadi, M. Haghshenas, Post heat treatment of additive manufactured AlSi10Mg: On silicon morphology, texture and small-scale properties, Mater. Sci. Eng. A. 783 (2020) 139296, https://doi.org/10.1016/j.msea.2020.139296.
[58] Y.S. Eom, J.M. Park, J.-W. Choi, D.-J. Seong, H. Joo, Y.C. Jo, K.T. Kim, J.H. Yu, I. Son, Fine-tuning of mechanical properties of additively manufactured AlSi10Mg alloys by controlling the microstructural heterogeneity, J. Alloy. Compd. 956 (2023) 170348, https://doi.org/10.1016/j.jallcom.2023.170348.
[59] X.X. Zhang, H. Andrä, S. Harjo, W. Gong, T. Kawasaki, A. Lutz, M. Lahres, Quantifying internal strains, stresses, and dislocation density in additively manufactured AlSi10Mg during loading-unloading-reloading deformation, Mater. Des. 198 (2021) 109339, https://doi.org/10.1016/j.matdes.2020.109339.
[60] P.C. Collins, D.A. Brice, P. Samimi, I. Ghamarian, H.L. Fraser, Microstructural control of additively manufactured metallic materials, Ann. Rev. Mater. Res. 46 (2016) 63–91, https://doi.org/10.1146/annurev-matsci-070115-031816.
[61] S. Bagherifard, N. Beretta, S. Monti, M. Riccio, M. Bandini, M. Guagliano, On the fatigue strength enhancement of additive manufactured AlSi10Mg parts by mechanical and thermal post-processing, Mater. Des. 145 (2018) 28–41, https://doi.org/10.1016/j.matdes.2018.02.055.
[62] F. Sausto, C. Tezzele, S. Beretta, Analysis of fatigue strength of L-PBF AlSi10Mg with different surface post-processes: effect of residual stresses, Metals 12 (2022) 898, https://doi.org/10.3390/met12060898.
[63] G. Di Egidio, L. Ceschini, A. Morri, M. Zanni, Room- and high-temperature fatigue strength of the T5 and Rapid T6 Heat-Treated AlSi10Mg alloy produced by laser-based powder bed fusion, Metals 13 (2023) 263, https://doi.org/10.3390/met13020263.